Semicond. Sci. Technol. 8 (1993) 80–87. Printed in the UK

TE and TM optical gains in AlGaAs/GaAs single-quantum-well lasers

E A Avrutin, I E Chebunina, I A Eliachevitch, S A Gurevich, M E Portnoi and G E Shtengel

A F Ioffe Physico-Technical Institute, 26 Polytekhnicheskaya Street, 194021 St Petersburg, Russia

Received 9 July 1992

Abstract. TE and TM optical gains were measured in AlGaAs/GaAs single-quantum-well (SQW) diode lasers at 300 K. Both the TE and TM gain spectra were step-like. The long and short wavelength steps in the experimental spectra were attributed to the onset of transitions from the first (e1) and second (e2) electronic subbands respectively. With increasing pumping current, the growth of the gain amplitude in the e1 transition slows down, the peak gain being approximately the same for TE and TM polarizations. On the contrary, the TE gain dominates over the TM gain in the e2 transition, which shows up at higher injection. Most of the polarization features of the observed gain spectra are easily interpreted within a model of direct optical transitions with the band mixing, relaxation broadening and bandgap shrinkage effects taken into account. At the same time, the gain saturation in the e1 transition observed in experiment can hardly be explained by the theory.

1. Introduction

Optical gain is a subject of special concern in studying the properties of QW lasers. In earlier papers [1–3] a simple parabolic band model was used to describe the optical gain in two-dimensional QW layers. In this model the energy levels of confined states in the conduction and valence bands were calculated using the bulk effective masses of electrons and holes, and the dispersion curves for the confined carriers were assumed to be parabolic. This leads to a step-like density of states. The energy- and polarization-independent momentum matrix elements for the optical transitions were taken to be the same as for the bulk material. In [4] a parabolic band approximation was also used, but the dependence of the matrix elements on the energy of carrier motion in the QW plane was introduced for the gain to become polarization-dependent. In recent studies [5, 6] the band mixing effect [7] was taken into account in calculations of the electron and hole wavefunctions in a QW. Band mixing appreciably changes the carrier dispersion law with respect to that obtained in a simple parabolic band approximation. In this approach the polarization and energy dependences of the momentum matrix elements can be described in a more rigourous way. In [4] the importance of intraband scattering for the description of the QW gain spectra was emphasized.

Several experimental techniques [8–11] have been used to measure the optical gain in QW active layers. The experiments showed a red shift of the long wavelength side of the QW gain spectra with an increase of the injected carrier density, which was attributed to the bandgap shrinkage [12]. In addition, a blue shift of the short wavelength side was associated with the band filling, which results in spectral broadening. The strong influence of the intraband relaxation on the gain profiles was well established experimentally from the appreciably smoothed maxima associated with different subband transitions. The intraband relaxation time in AlGaAs/GaAs QW layers was estimated to be $\sim 6 \times 10^{-14}$ s at 300 K by fitting the experimental and calculated gain profiles [9].

In spite of a large number of papers dealing with experimental and theoretical investigation of optical gain in QW lasers, the possibility for a correct description of TE and TM profiles and of the gain amplitude dependence on the carrier density is still questionable.

The main objective of this paper is to make a comparison of accurately measured TE and TM gain spectra with those calculated in the most reliable model of optical transitions in QW. In the calculations we used a model of direct transition with the band mixing, relaxation broadening and bandgap shrinkage effects taken into account. The gain spectra were measured by the Hakki and Paoli technique [13]. To get the best fit of the experimental and theoretical gain curves, the intraband relaxation time was used as the only adjustable parameter. In section 2 we describe the structure and some characteristics of SQW diode lasers used in the experiment. Then, details of the gain spectral measurement are discussed and experimental results are presented.

0268-1242/93/010080+08$07.50

In section 3 we discuss the results of a theoretical study of the gain spectra. Section 4 is for comparison of the experimental results with the theoretical predictions. In section 5 we summarize the results.

2. Laser structure, experimental technique and results

2.1. Laser structure and characteristics

Figure 1 shows schematically AlGaAs/GaAs separate confinement heterostructure (SCH), single-quantum-well (SQW), buried heterostructure (BH) lasers studied in the experiment. The laser fabrication process included MBE wafer growth and LPE mesa etch and re-growth. Initially, a buffer layer, a Si-doped n-$Al_{0.4}Ga_{0.6}As$ cladding layer ($1.0\,\mu m$; $n \simeq 1 \times 10^{18}\,cm^{-3}$), an undoped GaAs quantum well ($L_z \simeq 100$ Å) sandwiched between two undoped $Al_{0.2}Ga_{0.8}As$ waveguide layers (each $0.15\,\mu m$ thick), a p-$Al_{0.4}Ga_{0.6}As$ upper cladding layer ($1.0\,\mu m$; $p \simeq 1 \times 10^{18}\,cm^{-3}$) and a p^+-GaAs top layer ($0.5\,\mu m$; $p \simeq 1 \times 10^{19}\,cm^{-3}$), the latter two Be-doped, were MBE grown on a (100) n^+-GaAs substrate. The wafer surface was masked with $6\,\mu m$ wide SiO_2 stripes aligned in the [011] direction. Then the wafer was placed in an LPE reactor, where its surface was brought into contact with an unsaturated Ga+Al melt. After about 10 s of melt-back, the melt was removed and the resulting $3\,\mu m$ wide mesas were re-grown successively with n-$Al_{0.6}Ga_{0.4}As$, p-$Al_{0.4}Ga_{0.6}As$ and n-GaAs burying layers. The initial SiO_2 mask was removed and the surface, except for the mesa stripes, was covered with a SiO_2 blocking layer. Finally, metal contacts were deposited onto the top and bottom surfaces of the wafer.

Figure 2(*a*) shows the light output as a function of current for a fabricated SCH SQW BH laser diode ($400\,\mu m$ cavity length, 5 mA threshold current). One-side differential quantum efficiency is $\eta_d \simeq 20\%$ (uncoated mirrors). Figure 2(*b*) presents a far-field pattern parallel to the junction plane. A stable fundamental transverse mode operation of BH lasers can be seen up to the maximum output power. It should be noted that the threshold current density of a narrow mesa BH laser is equal to that of a broad-area SiO_2-confined $100\,\mu m$ stripe laser fabricated from the same MBE wafer with the same cavity length. This fact indicates a small current leakage in the fabricated BH laser structures. The threshold current density is $400\,A\,cm^{-2}$ for $400\,\mu m$ cavity length lasers.

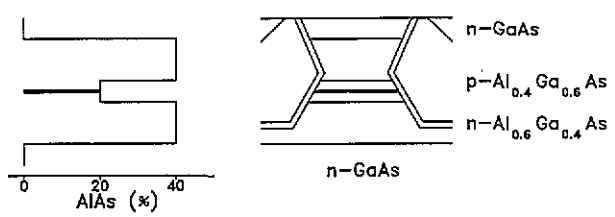

Figure 1. Schematic diagram of an AlGaAs/GaAs SCH SQW BH laser studied in the experiment. The thickness of the QW active layer is $L_z = 100$ Å.

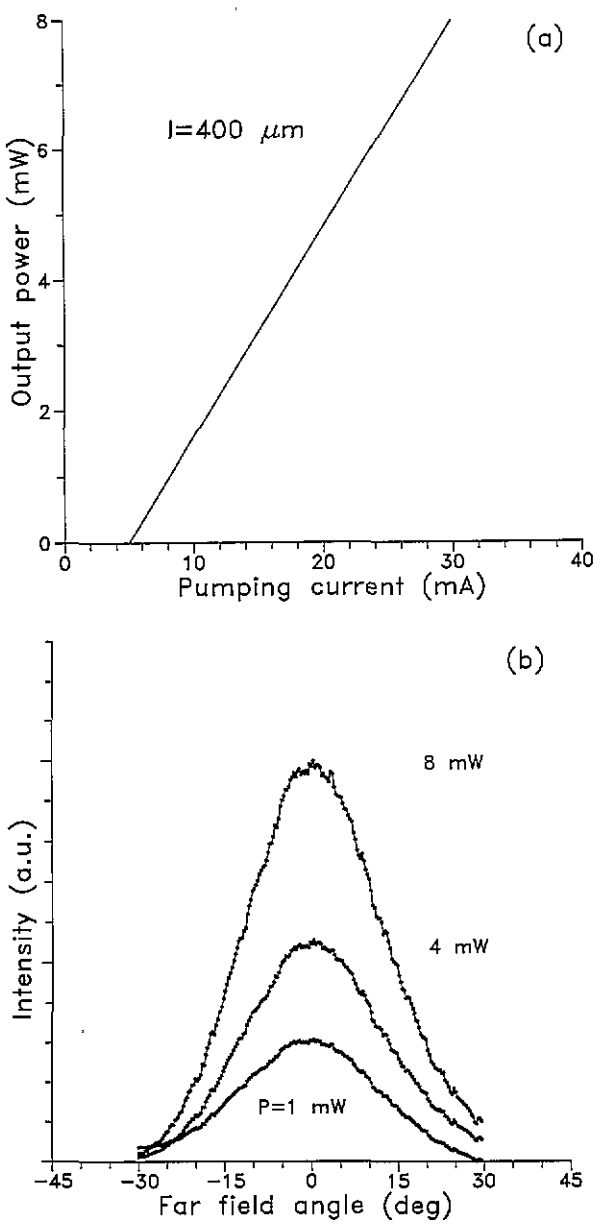

Figure 2. (*a*) Light output versus current. (*b*) Far-field pattern parallel to the junction plane at different output powers.

2.2. Experimental technique

The optical gain spectra were measured by the Hakki and Paoli technique [13]. In [13] the modal gain spectrum $G_m(\lambda)$ for a dominant mth transverse mode is given by

$$G_m(\lambda) - \alpha_i = \frac{1}{l}\left(\ln\frac{1}{R_m} + \ln\frac{\sqrt{r(\lambda)}-1}{\sqrt{r(\lambda)}+1}\right) \qquad (1)$$

where α_i is the distributed internal loss, l is the cavity length, R_m is the mirror reflectivity and $r(\lambda)$ is the maximum-to-minimum intensity ratio measured for each neighbouring peak and valley in the laser emission spectrum at the wavelength λ. Given l and R_m, the net gain, that is the difference $G_m(\lambda) - \alpha_i$, can be obtained directly from (1). Usually, the internal optical loss α_i is not known *a priori*. In BH lasers, α_i is supposed to be determined by the light scattering on the

laser waveguide imperfections and by the free carrier absorption, both mechanisms being weakly wavelength dependent. It is clear from (1) that at the long wavelength side of the emission spectrum, where the density of states vanishes, the modal gain will tend to zero, $G_m(\lambda) \to 0$, and the measured net gain value should tend to $-\alpha_i$. Besides, a specific feature of (1) is that at the laser threshold, when $r(\lambda) \to \infty$ at the emission peak, the net gain peak will tend to the cavity loss: $G_m(\lambda) - \alpha_i \to (1/l)\ln(1/R_m)$. Observation of the gain saturation at the laser threshold is a good means of testing the adequacy of experimental conditions when the Hakki and Paoli technique is used. The measured modal gain $G_m(\lambda)$ can be transformed to the material gain of the QW active layer $g(\lambda)$ with the optical confinement factor Γ_m: $g(\lambda) = G_m(\lambda)/\Gamma_m$. Generally, Γ_m is a polarization- and wavelength-dependent coefficient [14].

In the experiment the laser samples were pumped by 100 ns current pulses at a 50 kHz repetition rate. The sample heating during the current pulse was small, so the spectral line chirping did not limit the resolution. The average heating and the respective temperature shift of the spectra were also negligible. The radiation spectra were measured using a double monochromator (resolution limit of 0.03 nm), and a cooled GaAs photomultiplier. The laser emission was focused onto the input slit of the monochromator with a 50-fold magnification, so that the light emitted by the centre of the spot on the laser mirror was registered, while the light re-emitted in the GaAs substrate and cap layer was not detected. The size of the objective lens aperture was adjusted so as to be small enough to prevent the light scattered in the laser waveguide from affecting the registered spontaneous emission intensity [15]. In addition, a polarizer was used to separate the TE and TM polarizations.

2.3. Experimental results

Figure 3 illustrates a SCH SQW BH laser emission spectrum obtained at below-threshold pumping current. The inset in figure 3 shows a fragment of the emission spectrum extended in the horizontal scale. The fringe pattern is the result of constructive and destructive light interference in the laser resonator. By measuring the peak $P(\lambda)$ and valley $V(\lambda)$ intensities throughout the emission spectrum, one can get the interference function $r(\lambda) = P(\lambda)/V(\lambda)$, which is then used to calculate the gain spectrum by means of (1). This procedure was applied to the experimental TE and TM light emission spectra to obtain the TE and TM gains. When we used (1) to calculate the net gain, we took the laser mirror reflectivities to be $R^{TE} = 0.365$ and $R^{TM} = 0.270$ [14].

Figure 4 shows the experimental TE and TM gain spectra measured in a SCH SQW BH laser at different pumping currents below the laser threshold. The laser cavity length was rather small, $l \simeq 65\,\mu$m, so the maximum net gain was as large as 150 cm^{-1}, this value corresponding to the cavity loss. To study the gain spectra in a

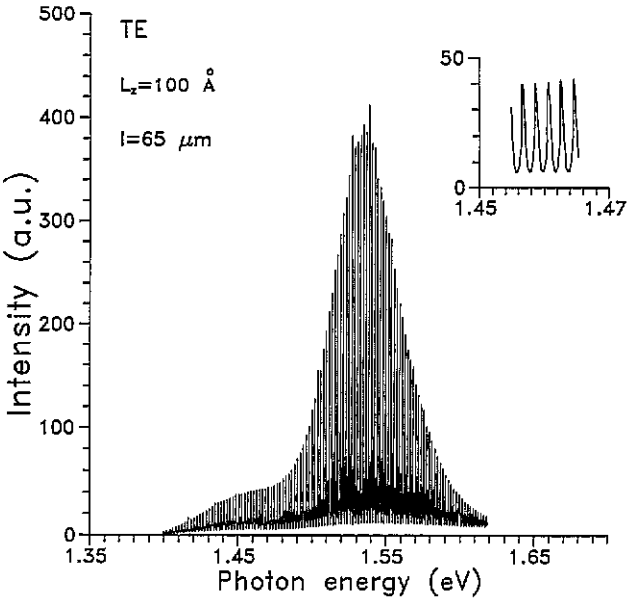

Figure 3. Emission spectrum of the AlGaAs/GaAs SCH SQW BH laser pumped below the threshold.

low gain range, it was more convenient to use a longer cavity laser. Figure 5 demonstrates the gain spectra measured in a laser with the cavity length $l = 220\,\mu$m, the corresponding cavity loss being $\simeq 40$ cm^{-1}. The internal losses can be evaluated from the TE spectra of figures 4 and 5 by measuring the zero gain level on the long wavelength wings of the curves. From these data the internal losses are $\alpha_i \simeq 20$ cm^{-1} for a short-cavity laser and $\alpha_i = 5$ cm^{-1} for a long-cavity one. The difference in α_i is likely to be due to casual variations in the intensity of light scattering by the waveguide imperfections. The influence of the free-carrier absorption in the QW active layer on α_i is expected to be small, since its contribution to α_i is scaled by the optical confinement factor $\Gamma_m \simeq 0.03$. As for the TM gain spectra in figures 4 and 5, they were not plotted sufficiently far in the long wavelength region, because in this region the light intensities were too small for an accurate gain measurement. This precluded the determination of the α_i level in the case of TM polarization.

The TE and TM gains in figure 4 have a step-like profile. The first step from the low photon energy side was attributed to the onset of transitions from the first electronic subband e1. The second step corresponds to the transition from the second subband e2.

For the interpretation of the experimental results, the energy levels of the confined states in the conduction and valence bands were calculated using the following structure parameters: the QW size $L_z = 100$ Å, the bandgap discontinuities at QW interfaces $\Delta E_c = 150$ meV and $\Delta E_v = 100$ meV. The fine structure associated with the heavy and light hole subbands involved in the transitions is unresolved in the observed spectra. Apparently, this is due to the smoothing, which results from the intraband relaxation broadening. It should be pointed out that the TE and TM gains in the e1 transition (long wavelength side of the spectra in figure 4)

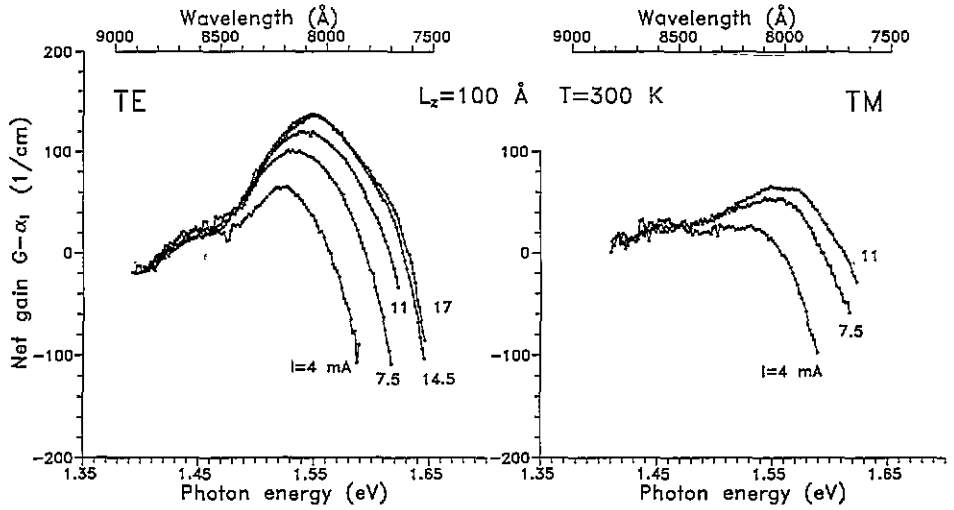

Figure 4. Experimental TE and TM net gain spectra at various injection currents. The laser cavity length is 65 μm (high gain).

have nearly the same amplitudes at the given pumping. These amplitudes are weakly dependent on the current. Increase in the current results in an appreciable rise of the gain at the short wavelength maximum associated with the e2 transition. In this transition the TE gain markedly dominates over the TM one. The increase of the TE gain in the e2 transition slows down at the laser threshold $I_{th} = 16$ mA, the peak net gain reaching the cavity loss level. The TM gain demonstrates a similar behaviour.

Figure 5 demonstrates the gain behaviour in the e1 transition in more detail. Here the TE and TM gains, having approximately the same amplitudes, increase slightly with increasing pumping. The TE gain peak becomes flatter, expanding up to the wavelength range, which corresponds to the e2 transition. The TM gain exhibits a similar distortion but under higher pumping (see figure 4). The TE gain curves from figure 5, recorded with the best accuracy, manifest a weak red shift of the long wavelength edge, which may be attributed to the bandgap shrinkage [12].

A characteristic feature of the spectra is a blue shift of the short wavelength side of the gain curves. This is associated with the band filling that occurs with the current increase. It is interesting to compare the positions of the short wavelength side of the TE and TM gain spectra at the same currents. One can see that the TE and TM curves cross the $-\alpha_i$ level at the same photon energy, which means that for both polarizations the condition $G = 0$ is fulfilled at the same spectral point. This coincidence should be expected if the gain is described in terms of the model of direct optical transitions with the same carrier temperatures in the conduction and valence bands [16].

3. Theoretical model and results

To obtain a quantitative interpretation of the experimental results, we have studied theoretically the gain

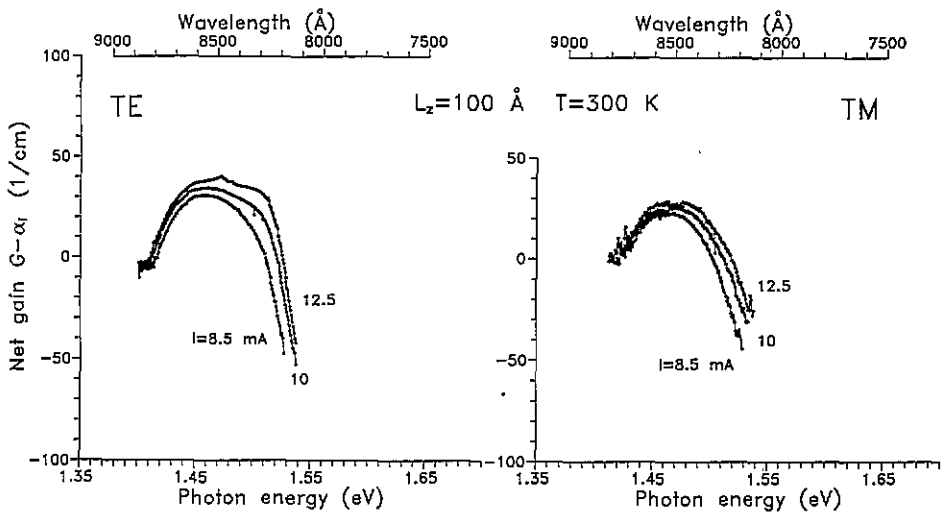

Figure 5. Experimental TE and TM net gain spectra of the laser with a 220 μm cavity length (low gain).

spectra for a QW with the parameters discussed above. The model we used in the computations was a well-known model of 2D momentum-conserving, relaxation-broadened interband optical transitions. In this treatment the material gain $g_\nu(\hbar\omega)$ for given light polarization ν (ν =TE or TM) and photon energy $\hbar\omega$ may be written as

$$g_\nu(\hbar\omega) = \frac{4\pi e^2 M_0^2}{n_{\text{eff}} m_0 c L_z \omega} \sum_{i,j,\alpha} \int \mathrm{d}(k^2) \beta_{i,j,\alpha}^{(\nu)}(k) \times \left[f_e(\epsilon_e^{(i)}) + f_h(\epsilon_h^{(j,\alpha)}) - 1 \right] \times \mathcal{L}(\hbar\omega - E_g - \epsilon_e^{(i)} - \epsilon_h^{(j,\alpha)}). \quad (2)$$

Here, n_{eff} is the effective refractive index and k stands for a value of the wavevector parallel to the QW plane. The indices i and j indicate the confined energy levels of electrons and holes respectively. The hole subbands are also assigned by the index α ($\alpha = \text{l}$ for a light hole and $\alpha = \text{h}$ for a heavy hole), the identification being made at $k = 0$. The factor $\beta_{ij\alpha}^{(\nu)}(k) = M_{ij\alpha}^{2(\nu)}(k)/M_0^2$ accounts for the k dependence of the interband matrix elements, M_0 being the bulk value. Then, f_e and f_h are the electron and hole Fermi functions. Finally, $\mathcal{L}$ is the joint spectral function of an electron–hole pair introducing relaxation broadening of the radiative transitions. We have used a simple form of $\mathcal{L}(\Delta\hbar\omega) = 1/\pi\gamma \times \sec(\Delta\hbar\omega/\gamma)$ [12] as a first approximation to a more complicated form computed numerically in [17, 18]. The carrier density-dependent bandgap is given by $E_g = E_{g0} - \Delta E_g$, where E_{g0} is the bandgap at zero carrier density. The bandgap shrinkage is introduced as $\Delta E_g = -E_{\text{Ryd}} a_0 / R_D$ [12], where E_{Ryd}, a_0 and R_D are the excitonic Rydberg energy, excitonic radius and Debye screening length respectively. The total electron and hole energies, $\epsilon_e^{(i)}$ and $\epsilon_h^{(j,\alpha)}$, which enter (2) as the arguments of the f_e, f_h and $\mathcal{L}$ functions, consist of two terms: $\epsilon_e^{(i)} = E_e^{(i)} + \Delta\epsilon_e^{(i)}(k)$ and $\epsilon_h^{(j,\alpha)} = E_h^{(j,\alpha)} + \Delta\epsilon_h^{(j,\alpha)}(k)$. Here, $E_e^{(i)}$ and $E_h^{(j,\alpha)}$ are the electron and hole energies at zero k, that is the energy level positions. The terms $\Delta\epsilon_{e,h}(k)$ are the momentum-dependent parts of the carrier energy.

A detailed form of the k dependences of $\Delta\epsilon_{e,h}(k)$ (electron and hole dispersion laws), as well as the exact values of $E_e^{(i)}$, $E_h^{(j,\alpha)}$, depend on the details of the theoretical model used, especially on the way the band mixing and the finite well barrier height are taken into account. We have assumed a simple parabolic dispersion law $\Delta\epsilon_e = \hbar^2 k^2 / 2m_e$ for electrons in a QW and an isotropic Luttinger model for the holes [19]. Here, the values of $E_e^{(i)}$ and $E_h^{(j,\alpha)}$ are not affected by the band mixing at all. On the contrary, the hole dispersion law is considerably changed by the band mixing but does not seem to depend too strongly on the barrier height, as long as the levels remain sufficiently deep. We therefore found it possible to calculate the $E_e^{(i)}$ and $E_h^{(j,\alpha)}$ energy level positions neglecting the band mixing. It was introduced only into computations of $\Delta\epsilon_h^{(j,\alpha)}(k)$ that were performed within the model of an infinitely deep well [7, 19]. The values obtained were then used to calculate $\beta_{i,j,\alpha}^{(\nu)}(k)$ by means of the analytical formulae derived in [19]. The results are plotted in figure 6 (hole dispersion law for an infinitely deep well) and figure 7 (matrix elements). A strong non-parabolicity of the valence band structure is seen in figure 6 with a region of negative effective mass in the lh1 subband. This results in a spike in the density of states. As seen in figure 7, the matrix elements corresponding to the transitions between the electron and hole subbands with different numbers are non-zero at $k \neq 0$. Some matrix elements behave non-monotonically with k, decaying to zero at large k values instead of the growth expected in the model of [4].

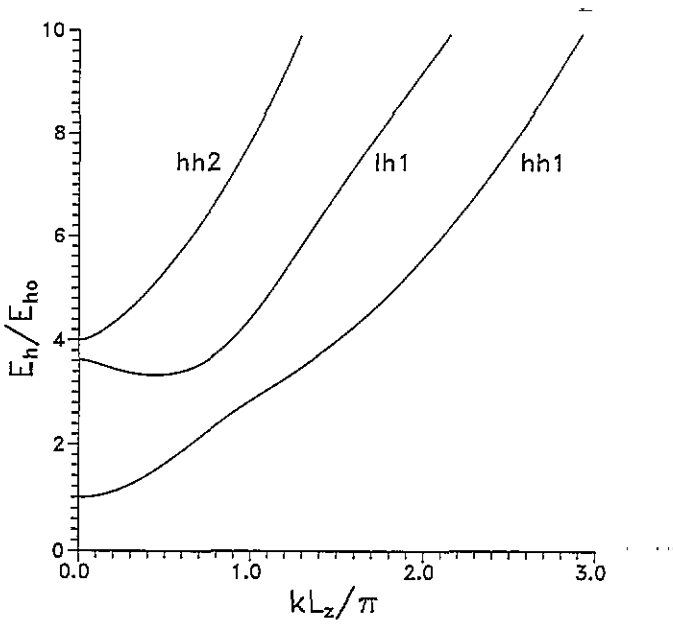

Figure 6. Calculated dispersion curves for three lowest hole subbands in an infinite well computed for the QW size L_z = 100 Å; k is the wavevector parallel to the QW plane. The hole energies are normalized by E_{h0}, i.e. by the hole energy in the first heavy subband at $k = 0$.

Figure 8 presents material gain spectra for both polarizations computed at a fixed carrier density ($N = P = 9 \times 10^{18}$ cm^{-3}) with and without relaxation broadening. It gives an insight into the contribution of transitions from different carrier subbands to the optical gain. A sharp spike observed in the gain curves is due to a spike in the density of states. But the relaxation broadening smooths down the sharp peaks in the gain spectra in figure 8 (broken curves). This figure also demonstrates a considerable difference in the TE and TM gain amplitudes in the high photon energy region corresponding to transitions from the $e2$ electron subband.

Figure 9 presents theoretical modal gains computed for different carrier densities. The relaxation broadening parameter was chosen to be γ = 12 meV to obtain the best fitting of the calculated and measured spectral profiles. As the gain spectra are broad, the wavelength-dependent optical confinement factors Γ_{TE} and Γ_{TM} were used to convert the material gain into a modal one. The calculated values of Γ_{TE} and Γ_{TM} appeared to

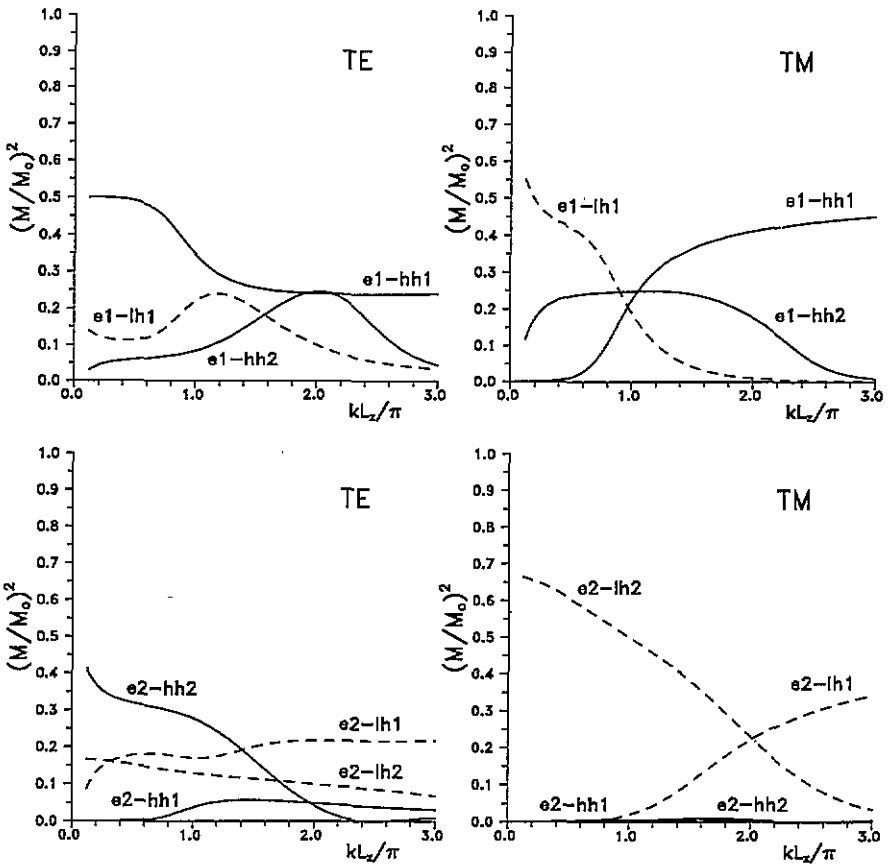

Figure 7. Calculated squared momentum matrix elements (normalized by the bulk value M_0^2) for radiative transitions between various subbands.

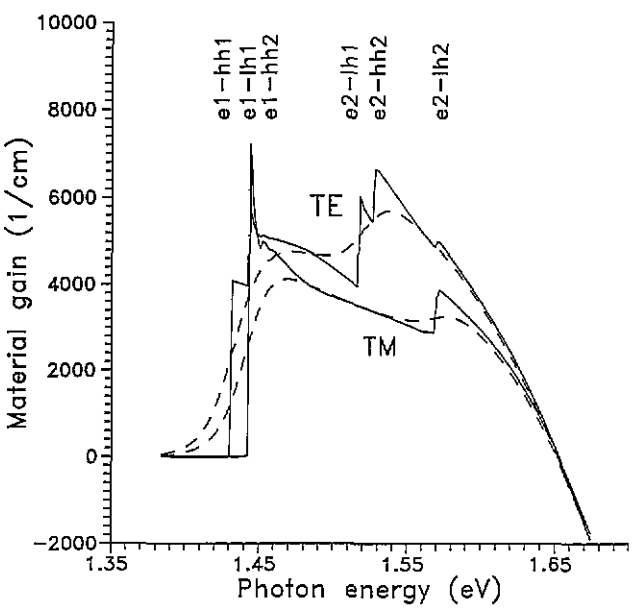

Figure 8. Calculated material gain spectra for TE and TM polarized light at $N = P = 9 \times 10^{18}\,\mathrm{cm}^{-3}$. Full curve: $\gamma = \hbar/\tau_{in} = 0$. Broken curve: $\gamma = 12\,\mathrm{meV}$.

be close, and ranged from 0.036 at the long wavelength side of the spectrum to 0.042 at the short wavelength side. The profile of the modal gains was found to be appreciably affected by the Γ factor dispersion.

As can be seen from figure 9, only transitions from the e1 level are important at a low carrier concentration. The gain spectra exhibit only one maximum, the peak values of G_{TE} and G_{TM} being close. As the carrier density is increased and higher-energy electron states become occupied, another peak is built up gradually at the high photon-energy wing of the spectrum. This peak is formed by transitions from the e2 subband. At a still higher carrier concentration it becomes dominant. The value of G_{TE} at this peak is considerably larger than G_{TM}, while the values at the low-energy (first-level) step remain close.

The polarization features of the calculated gain spectra may be explained semi-quantitatively in terms of the band mixing. For this, let us consider figures 6, 7 and 8, keeping in mind that with increasing photon energy $\hbar\omega$, different transitions are switched on at $\hbar\omega = E_g + E_e^{(i)} + E_h^{(j,\alpha)}$. For small photon energies, when only the e1–hh1 transition forms the gain, the TM matrix element is close to zero (figure 7), so the TE polarization dominates. At higher $\hbar\omega$, the e1–hh1 transitions are still active, but the onset of the e1–lh1 transitions makes the TE and TM gains approximately identical in amplitude. This identity holds for a considerable $\hbar\omega$ range, because at high k the band mixing reduces the difference between the TE and TM matrix elements for

all the transitions. Note that the relaxation broadening partially smooths down the difference between the TE and TM gains in a small photon energy range, below the onset of the e1–lh1 transition. The characteristic k value necessary for the band-mixing effect to be substantial is defined by the equation $k^2/q^2 \approx m_{lh}/m_{hh}$ [19] (q is the wavevector normal to the QW plane). In a spectral range corresponding to the transitions from the e2 subband, the e1 transitions form a gain plateau of approximately the same height for the two polarizations. It is onto this plateau that the gain caused by the e2 transitions is superimposed. For the carrier densities of interest, only the bottom of the e2 subband is occupied, determining a comparatively small k range available for the recombining carriers. As can be seen from the bottom of figure 7, for such k values the TM matrix elements are practically zero, except for the e2–lh2 transition, which works at fairly high photon energies, so it contributes to the gain only at the spectral edge. This is the reason why the TE polarization dominates in the high photon energy region (see figures 8 and 9).

4. Discussion

When comparing the experimental and theoretical gain spectra presented in figures 4 and 9, it might be more convenient to use pumping current as a common parameter for the two sets of curves. For this, the carrier concentration N (which is the parameter for the calculated gain spectra) could be converted to the pumping current with the expression $I = eR(N)L_z wl$, where L_z, w and l are the QW size, stripe width and cavity length respectively. The spontaneous emission rate $R(N)$ can be calculated using the carrier dispersion from figure 6 and the matrix elements from figure 7. We have calculated the current which should give a certain experimental gain amplitude. Unfortunately, this value has proved to be much lower than the experimental current value for the same gain. This means that in the experiment there is some excess current in the QW laser structure, which is generally associated with the non-radiative recombination at the QW interfaces [20] and with the carrier recombination in the waveguide layers [21]. For the same reason, the measured threshold current of QW lasers is in most cases higher than the calculated one [22]. So, we shall consider the theoretical gain calculated at different carrier concentrations and compare the experimental and theoretical profiles for approximately equal peak gain amplitudes. It should be pointed out that the theoretical model used in this study contains no fitting parameters, except for the relaxation broadening energy γ. This parameter was chosen to be $\gamma \simeq 12$ meV for the best fit with the experimental results.

It is evident from the comparison of figures 4 and 9 that some features of the experimental spectra can be well explained by the theory. In particular, at low photon energy corresponding to transitions from the e1 subband, the amplitudes of the TE and TM gains are similar when compared at the same pumping currents (figure 4) or at the same carrier concentrations (figure 9). At a high photon energy, where the transition from the e2 subband switches on, the TE gain is higher than the TM one. This is the case for both experimental and theoretical curves. The spectral position of the steps and the overall width of the gain spectra in figures 4 and 9 are also in reasonable agreement. However, considerable discrepancies remain in some of the details. The most important one is that the experimental gain in the e1 transition clearly saturates with the increase of pumping, which is much less pronounced in the calculated gain. A similar gain saturation in the e1 transition was observed earlier in [10]. The existing disagreement would be difficult to remove by using simple radiative transition models.

Indeed, at any reasonable carrier density, the holes would never reach a complete degeneracy. Therefore, the energy distribution function f_h in (2) will increase greatly with N, providing a gain increase in the entire spectrum. Obviously, the same result can be expected from a model neglecting the momentum-conservation law. Actually, no more detailed treatment of the band mixing in QW would be helpful in explaining the observed gain saturation. On the other hand, the theoret-

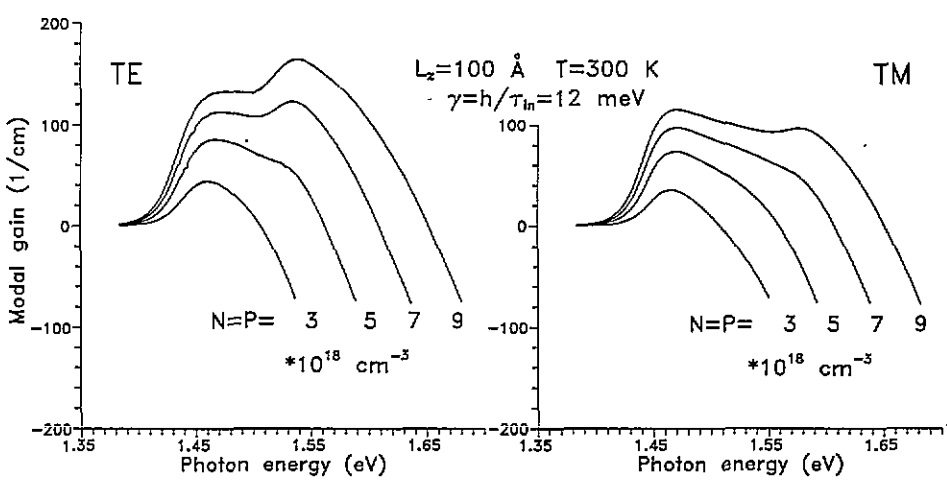

Figure 9. Calculated TE and TM modal gain spectra at various injected carrier densities.

ically predicted gain rise might be practically damped out by the increased free carrier absorption. But this assumption has not been proved by the experimental data in figure 4, where the loss level $-\alpha_i$ is clearly independent of the carrier density.

We believe that the observed gain behaviour can be qualitatively explained in the following way. Due to a comparatively small depth of the QW under consideration, a considerable carrier leakage in the barrier (waveguide) layers may take place under high pumping. If this is the case, the condition of the well neutrality ($N = P$) will be violated and the well bottom will not be flat, leading to transformation of the electron and hole wavefunctions and to a decrease of the matrix elements and, hence, of the gain [23]. This effect will be most significant at low photon energies, where the gain is formed by radiative transitions between the carrier states closest to the well bottom and increases with increasing pumping. Unfortunately, a quantitative treatment of such phenomena requires a far more complicated model with many-body effects taken into account.

5. Summary

The TE and TM optical gain spectra have been studied carefully in AlGaAs/GaAs SQW diode lasers at 300 K. A comparison has been made of the experimental gain spectra with those calculated in the framework of the most reliable model of direct transitions with the band mixing, including the relaxation broadening and bandgap shrinkage. In the low photon energy range corresponding to the transitions from the e1 subband, the experimental TE and TM gains have approximately the same amplitudes, which is due to the band mixing equalizing the TE and TM matrix elements. On the other hand, at higher photon energies the transitions from the e2 subband contribute primarily to the TE gain. In the experiment the gain increase in the e1 transition clearly slows down with increasing pumping. This gain behaviour cannot be adequately explained by the available theoretical models. A qualitative interpretation of this phenomenon has been suggested, taking into account the carrier leakage effect which distorts the charge neutrality and carrier wavefunctions in QW.

Acknowledgments

The authors would like to thank Dr F N Timofeev for designing the experimental set-up, Drs P S Kop'ev and V P Evtikheev for the sample preparation, and V V Dobretzov for the numerical calculations.

References

[1] Dutta N K 1982 *J. Appl. Phys.* **53** 7211
[2] Sugimura A 1984 *IEEE J. Quantum Electron.* **20** 336
[3] Arakawa Y and Yariv A *IEEE J. Quantum Electron.* **21** 1666
[4] Asada M, Kameyama A and Suematsu Y 1984 *IEEE J. Quantum Electron.* **20** 745
[5] Colak S, Eppenga R and Schuurmans M 1987 *IEEE J. Quantum Electron.* **23** 960
[6] Ahn D and Chung S 1990 *IEEE J. Quantum Electron.* **26** 3
[7] Diakonov M I and Khaetski A V 1982 *Zh. Eksp. Teor. Fiz.* **82** 1584
[8] Blood P, Fletcher E D, Hulyer P J and Smowton P M 1986 *Appl. Phys. Lett.* **48** 1111
[9] Zielinski E, Schweizer H, Hausser S, Stuber R, Pilkuhn M and Weimann G 1987 *IEEE J. Quantum Electron.* **23** 969
[10] Zhu L D, Zheng B Z, Xu Z Y, Xu J Z and Feak G A B 1989 *IEEE J. Quantum Electron.* **25** 1171
[11] Yamada M, Ogita S, Yamagishi M and Tabata K 1985 *IEEE J. Quantum Electron.* **21** 640
[12] Koch S W, Peyghambarian N and Gibbs H M 1988 *J. Appl. Phys.* **63** R1
[13] Hakki B W and Paoli T I 1975 *J. Appl. Phys.* **46** 1299
[14] Casey H C Jr and Panish M B 1978 *Heterostructure Lasers, Part A* (New York: Academic)
[15] Suris R A unpublished
[16] Lasher G and Stern F 1964 *Phys. Rev.* **133** A553
[17] Yamanishi M and Lee Y 1987 *IEEE J. Quantum Electron.* **23** 367
[18] Asada M 1989 *IEEE J. Quantum Electron.* **25** 2019
[19] Merkulov I A, Perel V I and Portnoi M E 1991 *Sov. Phys.–JETP* **99** 1202
[20] Iwata H, Yokoyama H, Sugimoto H, Hamo N and Onabe K 1988 *Digest of 11th Int. Semicond. Laser Conf.* (Boston US) paper C-6, p 42
[21] Alferov Zh I, Garbuzov D Z, Denisov A G, Evtikheev V P, Komissarov A B, Senichkin A P, Skorokhodov V N and Tokranov V E 1988 *Sov. Phys.–Semicond.* **22** 1331
[22] Alferov Zh I, Ivanov S V, Kop'ev P S, Ledentsov N N, Lutsenko M E, Mel'tser B Ya, Nemenov M I, Ustinov V M and Shaposhnikov S U 1990 *Sov. Phys.–Semicond.* **24** 152
[23] Livescu G, Miller D A B, Chemla D S, Ramaswang M, Chang T Y, Souer N, Gossard A C and English J H 1988 *IEEE J. Quantum Electron.* **24** 1677